Deep-Sea Research II 119 (2015) 30–39

Contents lists available at ScienceDirect

Deep-Sea Research II

journal homepage: www.elsevier.com/locate/dsr2

Seasonal variability in coastal fronts and its influence on sea surface wind in the Northern South China Sea

Rui Shi [a,*], Xinyu Guo [b], Dongxiao Wang [a], LiLi Zeng [a], Ju Chen [a]

[a] State Key Laboratory of Tropical Oceanography, South China Sea Institute of Oceanology, Chinese Academy of Sciences, 164 West Xingang Road, Guangzhou 510301, China

[b] Center for Marine Environmental Studies, Ehime University, 2-5 Bunkyo-cho, Matsuyama 790-8577, Japan

ARTICLE INFO

Available online 18 December 2013

Keywords:
Oceanic front
SST
Seasonal variation
SST–wind coupling
WRF model

ABSTRACT

High-resolution reanalysis data of Sea Surface Temperature (SST) show pronounced seasonal variations in oceanic fronts in the coastal area of the Northern South China Sea (NSCS), which are accompanied by the seasonality of monsoons. The NSCS oceanic fronts cover a wider area of the coastal sea in winter than in summer as strong winter monsoons progress. Nonetheless, the average SST gradients of the frontal area in both seasons are comparable. The response of surface wind to SST perturbations attributed to oceanic fronts in the NSCS coastal area has also been investigated by the observation data of satellite borne scatterometers and the simulation data of the Weather Research and Forecasting (WRF) model. Both the satellite observations and the simulations of the WRF model show apparent positive linear SST-wind coupling for most months in 2008, indicating the local influence of coastal SST fronts on the sea surface wind in the NSCS. The SST-wind coupling coefficients in the NSCS coastal sea are larger than those observed at mid-latitude oceans but smaller than those observed near equatorial oceans. It is also found that the influence of topography on the sea surface wind could be more important than that of the SST front at the southern end of the Taiwan Strait in winter. The transition of the monsoon could also affect the SST-wind coupling in the NSCS.

1. Introduction

For large scale ocean basins, Sea Surface Temperature (SST) perturbations are found to be negatively correlated with surface wind speed perturbations (Xie, 2004). Large-scale atmospheric circulation patterns change surface ocean temperatures through modulation of surface heat fluxes and surface mixed layer depth (Cayan, 1992). This is a one-way forcing of the ocean by the atmosphere. However, on smaller spatial scales between 100 and 1000 km, such as the mesoscale, the oceans drive an atmospheric response. In situ observations, satellite observations, and numerical simulations have consistently shown a positive correlation between surface wind speed and mesoscale SST variations (Small et al., 2008; Chelton and Xie, 2010).

An oceanic front is a typical mesoscale oceanic phenomenon identified by a discontinuity in temperature, salinity, or nutrient and chlorophyll *a* content (Belkin et al., 2009). SST perturbations associated with oceanic fronts can induce adjustment of the Marine Atmospheric Boundary Layer (MABL), and result in perturbations of the surface wind with enhanced winds over warm water and reduced winds over cold water. The responses of sea surface wind to SST perturbations over frontal areas are common in equatorial and mid-latitude oceans, including the eastern tropical Pacific (Wallace et al., 1989; Hayes et al., 1989; Chelton et al., 2001), the Kuroshio and its extension (Nonaka and Xie, 2003; Tokinaga et al., 2006), the Gulf Stream and its extension (Chelton et al., 2004; Song et al., 2006), the Brazil-Malvinas confluence in the South Atlantic (Tokinaga et al., 2005), and the Agulhas Current and Agulhas Return Current (O'Neill et al., 2005).

Previous studies have proposed several hypotheses to explain the mechanism of the surface wind response to oceanic SST fronts. One is the generation of hydrostatic pressure gradients through adjustments of the MABL mass fields (Lindzen and Nigam, 1987; Small et al., 2003; Song et al., 2006) and another is the stability-dependent modification of vertical mixing of momentum from aloft to the surface (Wallace et al., 1989; Hayes et al., 1989; Tokinaga et al., 2006). Tanimoto et al. (2011) proposed that both of these two mechanisms are active in the SST–wind interactions over a frontal area. Samelson et al. (2006) proposed an approximately linear relationship between the surface wind stress and the height of the MABL under a quasi-equilibrium condition, in which the MABL approximately comes into equilibrium with steady free-atmospheric forcing.

According to Yanagi and Koike (1987), oceanic fronts are classified into coastal water fronts, shelf fronts, and open ocean

* Corresponding author. Tel.: +86 208 902 4757.
E-mail address: shirui@scsio.ac.cn (R. Shi).

0967-0645/$ - see front matter © 2013 Elsevier Ltd. All rights reserved.
http://dx.doi.org/10.1016/j.dsr2.2013.12.018

fronts. A considerable number of studies on the relationship between SST and sea surface wind have been conducted on the continental shelf and the open ocean fronts in the equatorial and mid-latitude oceans. However, studies on the modification of sea surface wind via coastal water fronts have rarely been reported.

The South China Sea (SCS) is an epi-continental marginal sea of the western Pacific Ocean and a Mediterranean-type basin dominated by the Asian monsoon, which blows northeasterly from October to April and southwesterly from May to September in the northern regions of the SCS. The active coastal fronts observed in the Northern South China Sea (NSCS) vary throughout the year due to the combined effects of reversing monsoon winds, variations in bathymetry, and the tide (Wang et al., 2001; Hu et al., 2003; Liu et al., 2010). These shallow and narrow coastal fronts are accompanied by marked seasonal variations in strength and coverage. Thus, SST–wind coupling over coastal fronts in the NSCS could vary from those over open oceans.

In the present study, the seasonal variations in a NSCS coastal front and its influence on the sea surface wind in the NSCS are investigated. The observation data and the model configuration are described in Section 2. The seasonal variability of the NSCS coastal front and the observed SST–wind coupling induced by the front are demonstrated in Section 3.1. The verification of our one-year simulation is presented in Section 3.2, and the simulation results are used to analyze the SST–wind coupling. The analysis results are discussed in Section 4. Section 5 summarizes the study.

2. Data and model configuration

2.1. SST and wind data

The Operational SST and Sea Ice Analysis (OSTIA; Stark et al., 2007) data are provided by the Group for High Resolution SST (GHRSST) pilot project, which was initiated by the Global Ocean Data Assimilation Experiment in 2000. OSTIA uses several kinds of satellite data from the GHRSST project, as well as in-situ observations, to determine the SST for the global ocean. The combination of multi-sources in the OSTIA data eliminates some abnormal perturbations and generates a smooth SST map, which can be conveniently used by atmospheric models.

The OSTIA SST has a resolution of 0.05° at daily intervals. The OSTIA dataset provides robust data and acceptable accuracy near shores, which enables it to identify coastal fronts in the NSCS. Xie et al. (2008) estimated five types of SST products of the GHRSST project and found that the OSTIA SST yields the smallest Root Mean Square Difference (RMSD) compared to the independent buoy and ship observations in the coastal and shelf seas around China.

The sea surface wind data used in this study were observed by Quick Scatterometer (QuikSCAT) and Advanced Scatterometer (ASCAT). Thus far, QuikSCAT provides a more extensive geographical and temporal coverage and higher spatial resolution of the ocean vector winds compared to those obtained by other spaceborne sensors (Chelton and Wentz, 2005). After QuikSCAT finished its mission in October 2009, ASCAT continues to provide global sea surface wind data. These two kinds of wind data have been widely used in previous studies on SST–wind coupling over open ocean fronts (Chelton et al., 2001; Nonaka and Xie, 2003; Tokinaga et al., 2006; Song et al., 2006; O'Neill et al., 2005, 2010; O'Neill, 2012).

The QuikSCAT data from 1999 to 2009 are distributed by Remote Sensing Systems (RSS). The ASCAT data from 2009 to 2011 are available from the Asia-Pacific Data Research Center. Despite missing near-shore data, the existing data covering the NSCS frontal area are sufficient to support the present study. Similar to previous studies, the analysis in this study that utilizes wind data is based on 10-m equivalent neutral winds. Equivalent neutral wind is the wind that would exist for an idealized condition at a given height if the atmospheric boundary layer was neutrally stratified.

2.2. Model configuration

The Weather Research and Forecasting (WRF) model with the Advanced Research WRF (ARW) dynamic solver (Skamarock et al., 2005) is used to confirm the response of sea surface winds to mesoscale SST perturbations over the NSCS coastal fronts. The WRF model has been used in previous studies to examine air–sea coupling processes over oceanic fronts (Song et al., 2009; O'Neill et al., 2010).

The WRF model in this study has two nested domains, D1 and D2, with horizontal resolutions of 18 and 6 km, respectively. The outer domain (D1) covers the NSCS while the inner domain (D2) focuses on the southern coastal area of China (Fig. 4A). Two-way nesting is applied to allow interactions between the two domains. This study used the simulation results of D2.

Two domains were initialized with the National Centers for Environmental Prediction (NCEP) operational analysis data. The lateral boundary conditions for D1 were updated by NCEP analysis data every 6 h to allow large-scale synoptic weather systems outside of the domain to propagate through the domain. Daily OSTIA SST data, which were updated every 24 h during the simulation periods, were used as the bottom boundary condition. The initial and boundary conditions were designed to obtain a realistic simulation result and to maintain consistency in the analysis of the observation and simulation results.

The simulation was performed using 43 vertical sigma levels including 25 levels below 1000 m. A fine vertical resolution was specified in the boundary layer to accurately simulate the vertical turbulent momentum exchange in the layer. The lowest level extends from the surface to a height of 12 m, whereas the highest level almost reaches a height of 20 km.

An improved Mellor–Yamada–Nakanishi–Niino (MYNN) level 3 scheme is employed to simulate the marine atmospheric boundary layer. This scheme is based on the original Mellor–Yamada level 2.5 turbulence closure model (Mellor and Yamada, 1982) and imposes additional restrictions to assure its reliability and numerical stability (Nakanishi and Niino, 2006). The Noah land surface model is also adopted in the simulation. The microphysical parameterizations include explicitly resolved water vapor, cloud, and precipitation processes. A modified version of the Kain–Fritsch scheme is used to represent the subgrid-scale effects of convection and shallow clouds.

The model was run for an integration period of one month, starting at 0000 UTC on the first day of the month and ending at 2400 UTC on the last day of the month. This process was conducted for the 12 months of 2008 to investigate the influence of fronts on sea surface winds during different seasons.

3. Results

3.1. Observation

3.1.1. Seasonal variability of the SST front

The monthly mean magnitude of the SST gradient was calculated using the OSTIA data from 2006 to 2011. The magnitude of the SST gradient can be regarded as an index of the strength of the coastal fronts. Therefore, maps showing the magnitude of the SST gradient were used to investigate the spatial distribution and seasonal variation of the SST front.

Visual examination suggests that coastal fronts mainly occur in three areas in the NSCS where the magnitude of the SST gradient is greater than 0.005 °C km^{-1} (Fig. 2). The three areas are located in Beibu Bay, the southeastern coastal area of mainland China (SCC), and off the northwest coast of Luzon Island (see Fig. 1 for the geographic locations). Fronts in the SCC area appear regardless of

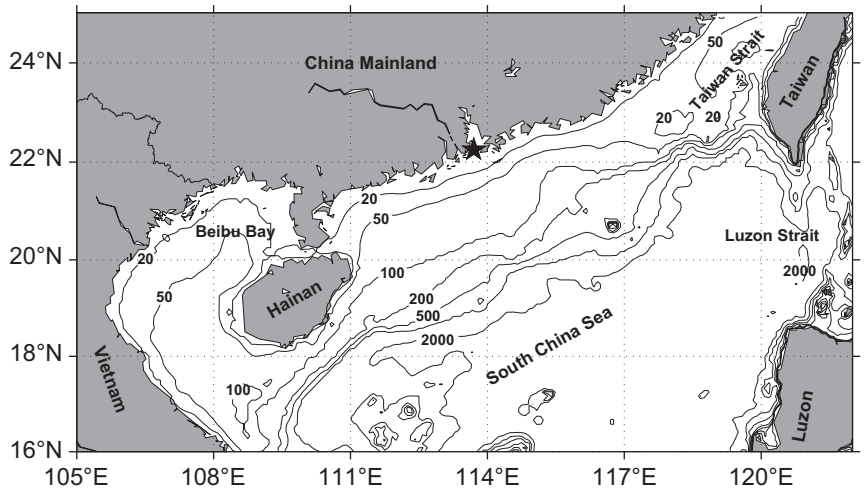

Fig. 1. Map of the northern South China Sea with bathymetry contours (m). The star denotes the Pearl River estuary.

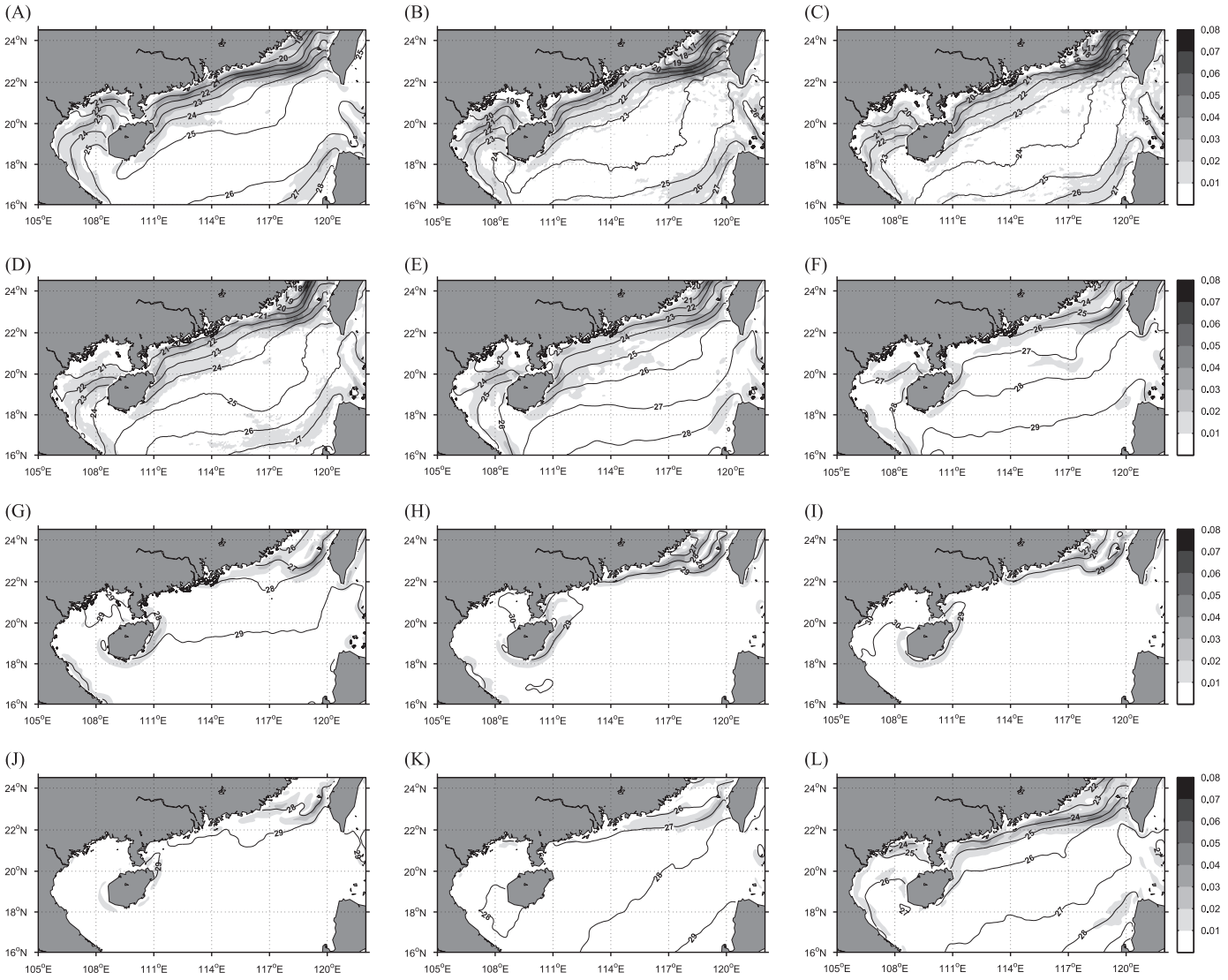

Fig. 2. Monthly mean SST (black contours, °C) and the magnitude of the SST gradient (shaded gray area, °C km^{-1}) calculated by using the OSTIA data from January 2006 to December 2011.

the season, whereas fronts in the Beibu Bay and off the northwest coast of Luzon Island occur only in winter and disappear in summer. Therefore, the following analysis was mainly performed in the SCC area (111–120°E, 19–24.5°N).

During winter, a SST front expands across most of the SCC. This front starts to develop in November (Fig. 2l), enters its mature stage in December (Fig. 2A), and gradually weakens in March (Fig. 2D). In winter, the SST gradient is generally weaker in the western portion of the SCC than in the eastern area near the Taiwan Strait. The eastern SST gradient of the SCC is stronger both in January and February than in December, and the western SST gradient varies slightly in winter (Fig. 2A–C).

The summer front begins to form in June (Fig. 2G), develops in July and August (Fig. 2H and I), and weakens in September (Fig. 2J). In summer, apparent fronts appear only in the eastern part of the SCC. Thus, the area covered by the front is smaller in summer than in winter. Compared to the winter front, the summer front is restricted to a shallower sea that is close to the coastline. Notably, fronts at the southern end of the Taiwan Strait are observed during all seasons and apparently weaken in summer. A maximum value of over 0.07 °C km^{-1} for the SST gradient is observed in this area in January and this value decreases to approximately 0.06 °C km^{-1} in July.

For a quantitative analysis of the seasonal variation in coastal fronts in the SCC, grid points were specified to cover the frontal area. The contour of the 23.5 °C isotherm in the SCC in December (Fig. 2A) was chosen as the center line of the area covered by grid points. Thirty-seven grid points were first given at every quarter degree along the contour of the 23.5 °C isotherm. From each grid point along the line, four grids were then specified in intervals of 0.25° along both sides normal to the line. Finally, an array of 37 × 9 grids covering an area of 9° × 2° in the SCC was obtained (see dots in Fig. 4A). The coverage and the mean strength of the front were calculated based on the area covered by these grid points.

The coverage of the front was defined by the percentage of grid points with a SST gradient magnitude greater than 0.005 °C km^{-1}. The SST front covers 80% of the SCC area in winter and does not change significantly from January to April (Fig. 3A). However, an abrupt reduction is observed in the covering rate from 80% to 40% in May, and a continuous reduction to about 30% in June. The coverage increases slightly in July and then decreases again in August. The front covers only 20% of the SCC area in September, which is the minimum value of coverage for the entire year (Fig. 3A).

The magnitudes of the SST gradient at each grid point were averaged in the frontal area mentioned above. The mean magnitude of the SST gradient does not change as significantly as the coverage of the front does in different months (Fig. 3B). In general, the mean magnitude of the SST gradient associated with a well-developed front is stronger in winter than in summer, decreasing by approximately 0.004 °C km^{-1} from 0.021 °C km^{-1} in January to 0.017 °C km^{-1} in July (Fig. 3B). The mean magnitude of the SST gradient does not decrease as abruptly as the coverage of the front does in May. Instead, the mean magnitude decreases gradually from January to June, slightly increases in July, and decreases again until October (Fig. 3B).

The seasonal variability of a front in terms of spatial distribution and strength could induce different responses of sea surface wind. The potential effects are discussed in the subsequent section.

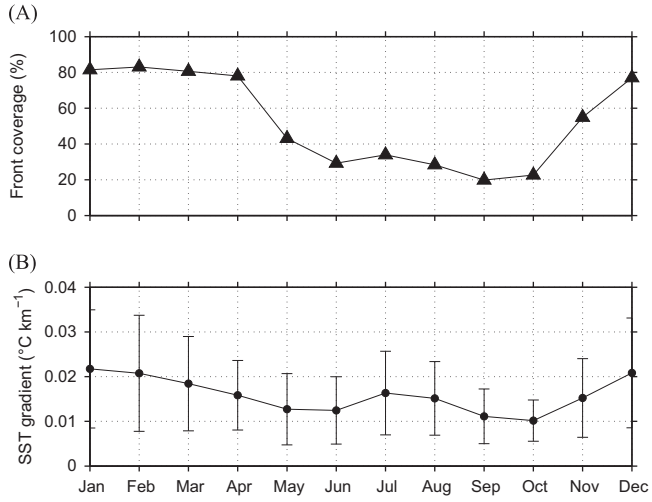

Fig. 3. Two statistical parameters of the SST fronts at the grid points shown in Fig. 4a: (A) seasonal variations in the coverage rate of the fronts (black triangles), and (B) mean values (black dots, °C km^{-1}) and ±1 standard deviation (vertical bars) of the magnitudes of the SST gradient for each month. The grid points where the SST gradient was smaller than 0.005 °C km^{-1} were not included in (A) and (B).

3.1.2. *Observed SST–wind coupling*

The monthly averaged SST and wind field are shown in Fig. 4B for December 2008, which is a representative time period to study the influence of a SST front on the sea surface wind in the NSCS. During this period, the entire domain was covered by the strong northeasterly monsoon, and an apparent front parallel to the coastline can be identified. Along this front, the wind speed was high over the warm water side and low over the cold water side of the front, which is an indication of the positive correlation of SST–wind coupling (Chelton and Xie, 2010). This positive correlation is presented more clearly in the meandering of the front around

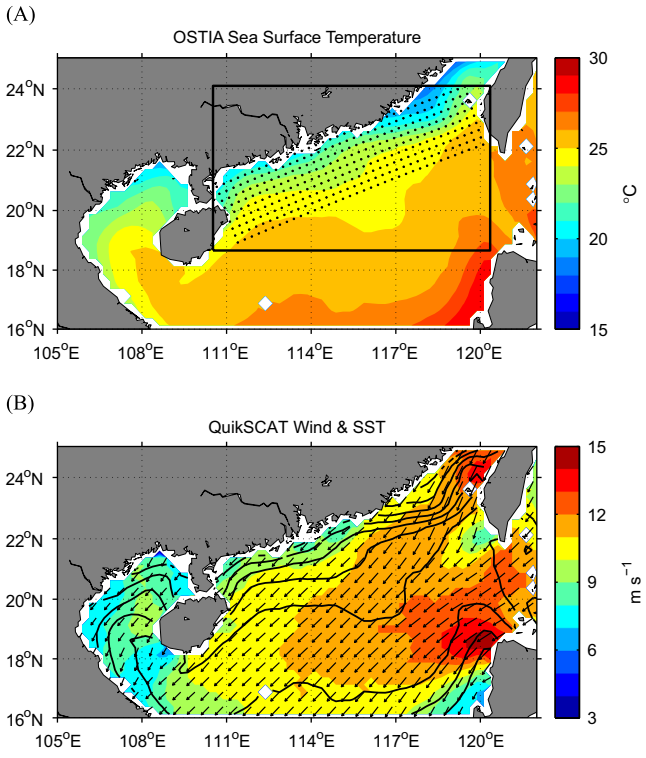

Fig. 4. (A) Monthly mean SST obtained from the OSTIA data for December 2008, and (B) the QuikSCAT equivalent neutral winds at 10 m height (black arrows) and wind speeds (shaded tone, m s^{-1}) overlaid by the OSTIA SST contours from 18 °C to 28 °C at an interval of 1 °C. The original OSTIA SST with a horizontal resolution of 0.05° was interpolated to the QuikSCAT grid points. The area enclosed by the black box in (A) is the inner nest domain of the WRF model. The black dots in (A) are the grid points covering the most active frontal area in the NSCS and are defined in Section 3.1.

20°N, 116°E (Fig. 4B). However, no evidence was observed for a similar positive SST–wind coupling at the south end of the Taiwan Strait and off the northwest coast of Luzon Island.

Previous studies show that the removal of large-scale fields by spatial high-pass filtering provides an intuitive presentation of the coupling of perturbation fields (Chelton et al., 2001; Nonaka and Xie, 2003). The same method was slightly modified and applied in the present study. A spatial filter of nine grids in the direction across the front and three grids in the direction along the front was constructed using a Gaussian smoothing function. Spatially high-pass-filtered fields at the grid points were obtained by removing spatially low-pass-filtered fields with the Gaussian smoothing function. Spatially high-pass-filtered fields are hereinafter referred to as perturbation fields.

In winter, the perturbations of SST and sea surface wind have the same sign over the frontal area west of 117°E (Fig. 5A, B, and L), indicating a positive correlation of SST–wind coupling. There was an asymmetric perturbation of the SST on the cold and warm sides of the SST front, which also corresponds to an asymmetric perturbation of surface wind. The negative SST perturbation varies from −0.05 to −1.5 °C, whereas the positive SST perturbation varies from 0.05 to 0.5 °C. The positive perturbation of sea surface wind is about 0.05 to 0.5 m s^{-1} over warm water and −0.05 to −0.75 m s^{-1} over cold water (Fig. 5A, B, and L). Thus, the perturbations of surface wind are larger over cold water than over warm water.

However, the positive SST–wind correlation in winter could be overlaid by the influence of terrain in the area east of 117°E, where the perturbed SST and wind have opposite signs (Fig. 5A, B and L). The narrowing effect of the Taiwan Strait intensifies the sea surface wind speed inside the Taiwan Strait and weakens it off the south end of the Taiwan Strait (Fig. 4B). Meanwhile, the blocking effect of Taiwan Island reduced the sea surface wind speed along the southwest of Taiwan Island (Fig. 4B). The joint effect of these two topographic factors was more significant than the influence of the SST front in this area. Therefore, there was a negative SST perturbation overlaid by a positive wind speed perturbation in the Taiwan Strait and a positive SST perturbation overlaid by a negative wind speed perturbation along the southwest coast of Taiwan Island.

On the other hand, the positive SST–wind correlation can also be observed in the area east of 117°E in June, July, and August (Fig. 5F–H) when the SST front has a small but well-developed range (Fig. 2G–I). During this season, the wind direction reverses

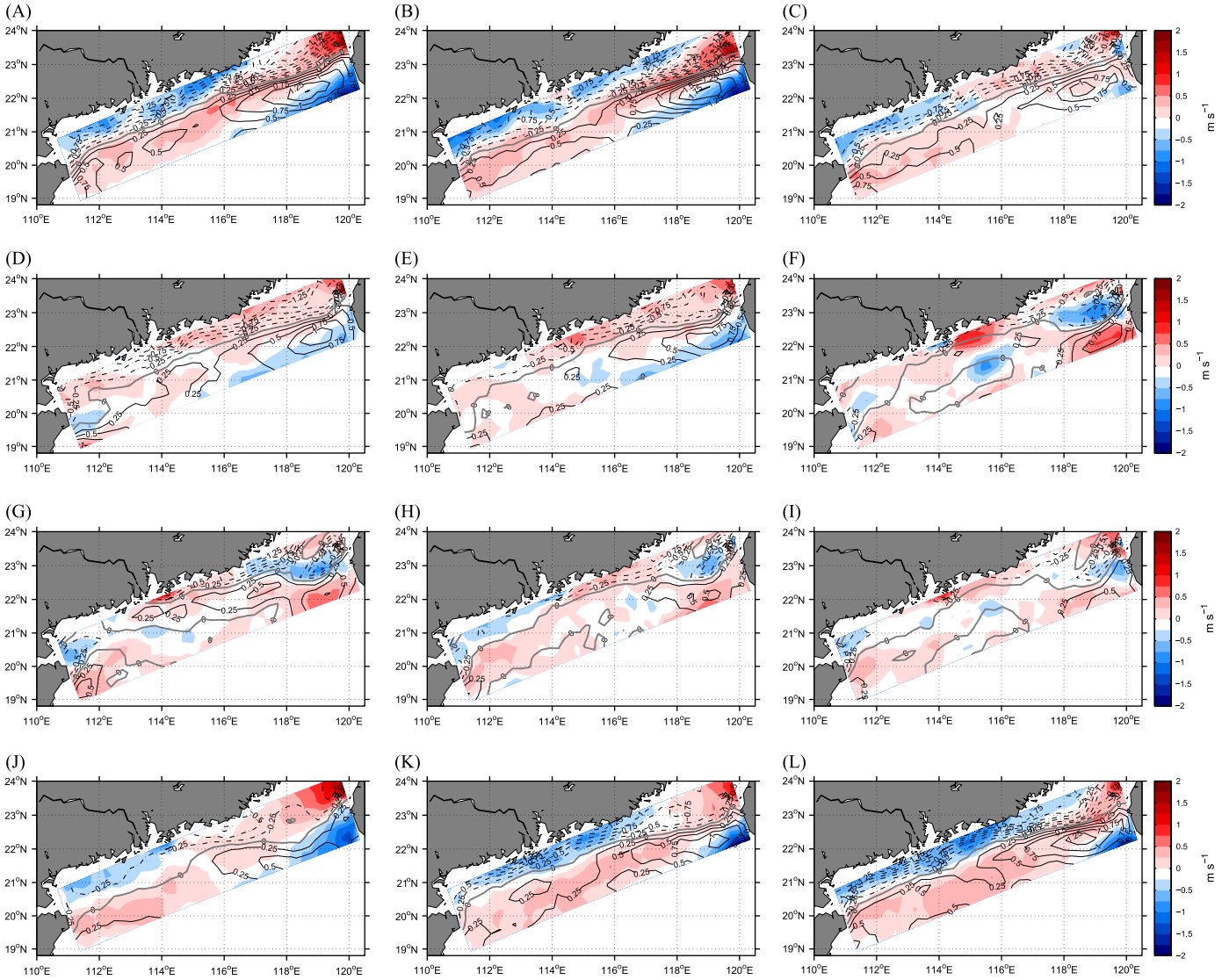

Fig. 5. Spatially high-pass-filtered monthly mean values of the OSTIA SST (°C) overlaid as contours on the spatially high-pass-filtered monthly mean values of the QuikSCAT equivalent neutral wind speeds (m s^{-1}) at 10 m height from January 2008 to December 2008. Positive and negative high-pass-filtered SSTs are denoted by solid and dashed lines, respectively, at an interval of 0.25 °C. Gray lines denote a zero high-pass-filtered SST. Description of the high-pass filter is given in Section 3.1.

and the topographic effects are little. Thus, the positive SST–wind correlation becomes most apparent at the southern end of the Taiwan Strait, where the SST gradient is much stronger than the other areas in the NSCS in summer. However, this relationship is rarely observed in the months when the monsoon season begins, such as April, May, and September (Fig. 5D, E, and I), since the frequent changes in wind direction caused by the unstable prevailing monsoon make it difficult to identify the influence of the SST perturbation on the sea surface wind.

3.2. Model simulation

3.2.1. Validation of simulation results

A one-year realistic simulation using the WRF model was carried out to reproduce the observed SST–wind coupling process in the NSCS in 2008. The simulation is considered a one-way coupling of SST and wind, which simplifies the complex ocean dynamical processes to be represented by updating the daily SST. The performance of the WRF model was evaluated before further analysis. The monthly mean wind speed and direction at a height of 10 m were simulated by the WRF model and interpolated to the spacing of the grid points at 25 km. These were then compared to the QuikSCAT data of the same domain.

The model successfully simulated the spatial pattern of the sea surface wind in the NSCS in December 2008 (Fig. 6B). The vector mean of the simulated wind direction was highly consistent with the observations. However, the mean of the simulated wind speed was about 1 m s^{-1} lower than that of the observations. The underestimation of wind speed by the model could be considered negligible because the observed mean wind speed was generally greater than 10 m s^{-1} in this area.

A quantitative evaluation of the surface wind simulated by the model for each month in 2008 was performed. Two statistical parameters, the RMSD of the wind speed at 10 m height and the mean absolute error (MEAN) of the wind direction at 10 m height, were calculated by using the following equations:

$$RMSD = sqrt\left(\sum_{i=1}^{N}(X_{mod}^{i}-X_{obs}^{i})^{2}/N\right) \quad (1)$$

$$MEAN = \sum_{i=1}^{N}|X_{mod}^{i}-X_{obs}^{i}|/N \quad (2)$$

where X_{mod} denotes the variable from the model results, X_{obs} is the corresponding variable of the satellite observations, N is the data number, and i is the grid number. The RMSDs of the wind speed between the model results and the observation data were ~1 m s^{-1} during most months and less than 1 m s^{-1} during the summer (Table 1). Meanwhile, the MEANs of the wind direction were less than 10° during most months (Table 1). Given that all the

Table 1
Comparison between the winds simulated by the WRF model at 10 m height and the QuikSCAT observed equivalent neutral winds at 10 m height from January 2008 to December 2008. See the text for the definitions of RMSD and MEAN.

RMSD of wind speed (m s^{-1})											
1.09	1.15	0.72	0.92	0.62	0.52	0.52	0.77	0.73	1.26	1.03	0.89
MEAN of wind direction (deg)											
6.05	5.95	10.24	21.5	46.41	7.58	6.56	12.99	18.3	8.38	3.93	4.23

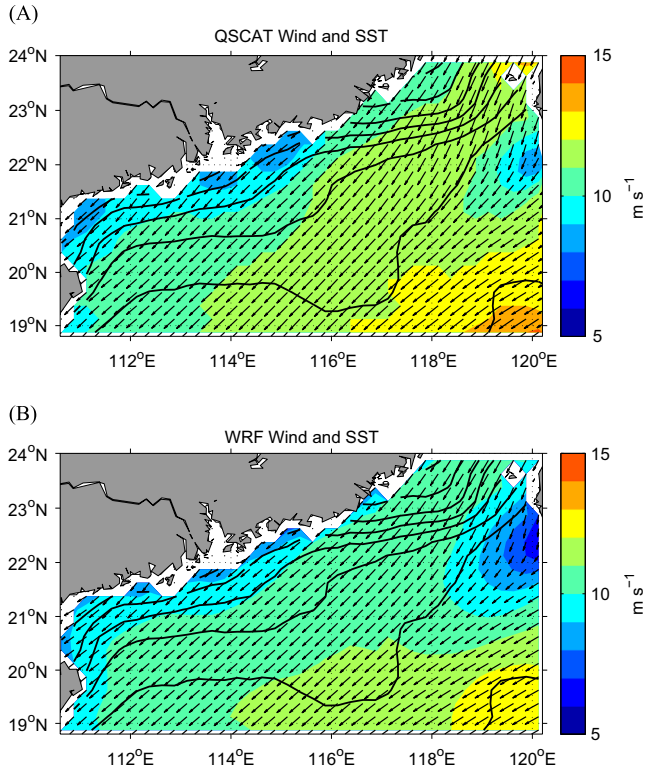

Fig. 6. (A) Monthly mean values of the QuikSCAT equivalent neutral winds (black arrows) and their speeds (m s^{-1}, color tone) at 10 m height in December 2008. (B) The same as (A) but for the winds simulated by the WRF model. (A) and (B) are overlaid by the monthly mean SST contours (black lines) from 18 °C to 28 °C at an interval of 1 °C.

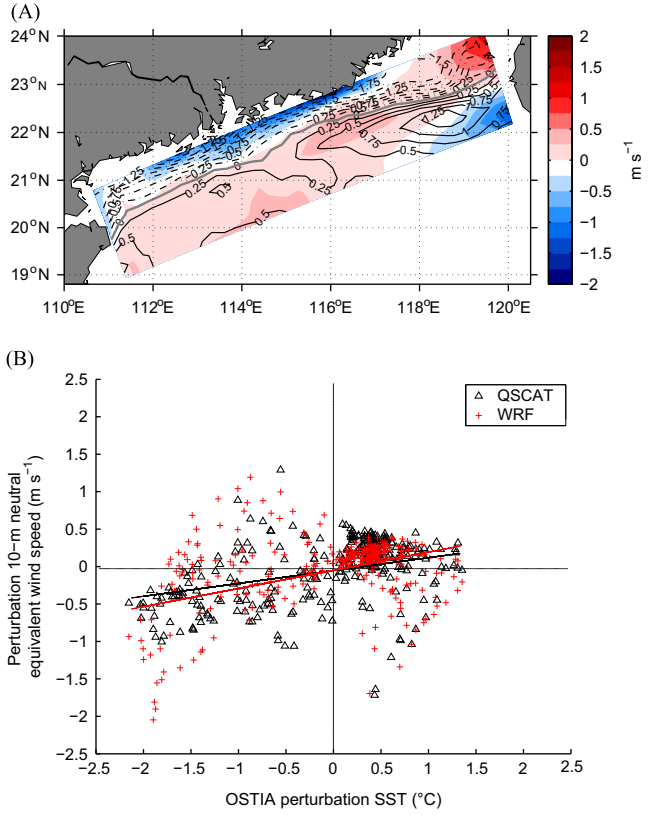

Fig. 7. (A) Spatially high-pass-filtered OSTIA SSTs (contours, °C) and spatially high-pass-filtered wind speeds (color tone, m s^{-1}) at 10 m height as simulated by the WRF model in December 2008. (B) Scatter plot of the spatially high-pass-filtered wind speeds versus the spatially high-pass-filtered OSTIA SSTs for the data shown in panel (A) (crosses) and for those shown in Fig. 5L (triangles).

simulations were conducted without data assimilation and the simplification of oceanic processes, the performance of the model was acceptable for the subsequent analysis.

3.2.2. Simulated SST–wind coupling

In Fig. 7A, the perturbation of the OSTIA SST is overlaid as contours on the perturbation of the surface wind speed simulated by the WRF model for December 2008. The model generated a similar spatial map of the observed SST–wind coupling shown in Fig. 5L. The perturbations of the SST and the sea surface wind bear the same sign in the area west of 117°E and opposite signs in southern end of the Taiwan Strait. The sea surface wind perturbation is also larger over cold water than over warm water (Fig. 7A), indicating that the reduction in surface wind speed over cold water is more significant than the increase in surface wind speed over warm water.

The SST-induced change in the surface wind speed in December 2008 can be statistically analyzed in the scatter plot of the surface wind perturbations as a function of the SST perturbations (Fig. 7B). Both the simulation results and the observation results show a similar positive linear relationship between the perturbations of SST and sea surface wind (Fig. 7B). The scatter plot exhibits a higher concentration in the first quadrant than in the third quadrant because the positive perturbation of the SST varies over a small range (Fig. 7A). Meanwhile, the plots in the second and fourth quadrants illustrate the opposite signs of the perturbations of the SST and surface winds in the area east of 117°E (Fig. 7A).

In Section 3.1.2, the observed SST and sea surface wind perturbations showed that the positive SST–wind coupling can be observed in the different frontal areas accompanied by the changes in season (Fig. 5). Therefore, the monthly scatter plots of the SST and sea surface wind perturbations were carried out in the apparent coupling area to investigate the seasonal variations of the coupling (Fig. 8).

Both the results of the WRF model and the observation show apparent positive linear SST–wind coupling during most months with variations in the coupling coefficient, which is defined as the slope of the least-square regression line (Fig. 8). In general, the coupling coefficients obtained by the simulation and observation range from about 0.27 to 0.5 (Table 2), which is larger than the coupling coefficients observed over the Gulf Stream but smaller than those observed over the equatorial Pacific (O′Neill, 2012).

The SST–wind coupling coefficients are a little larger in November and December than in June and July (Table 2), despite the significant difference in their spatial size. However, the coupling coefficients are

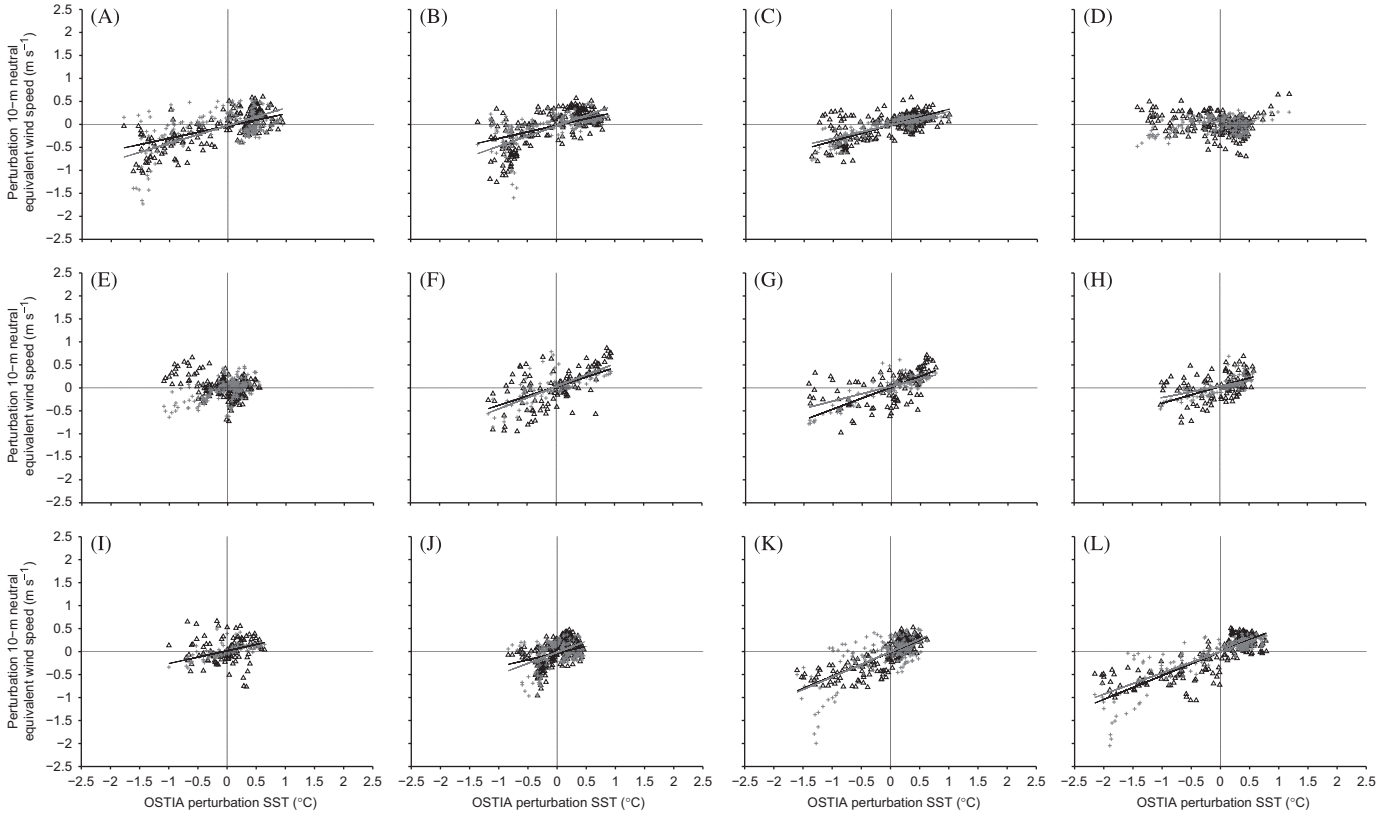

Fig. 8. Scatter plot for the spatially high-pass-filtered monthly OSTIA SST (°C) and surface wind speed (m s^{-1}) in the area east of 117°E for June, July, August, and September (F, G, H, I), and in the area west of 117°E for the other months. Gray crosses and black triangles denote the WRF simulation results and the QuikSCAT observation data, respectively. Gray and black lines represent the linear least-squares fitting for the scatter plot of the WRF model results and QuikSCAT observations, respectively.

Table 2
Coupling coefficients from the scatter plots for the SST and sea surface wind speed perturbations in the frontal areas from January 2008 to December 2008 (Fig. 8). The symbol "–" denotes the coupling coefficients that did not pass the confidence test.

	Coupling coefficient											
WRF	0.27	0.29	0.35	–	–	0.41	0.48	0.37	0.28	0.30	0.52	0.52
QuikSCAT	0.39	0.45	0.30	–	–	0.50	0.32	0.25	0.07	0.48	0.55	0.46

smaller in January and February than in June and July. The SST–wind coupling is weak or difficult to identify during the transition periods to the monsoon season in April, May, and September.

4. Discussion

The seasonal variability in the coastal front in the NSCS is significant, particularly along the southeastern coastline of China. A simple explanation is presented by considering the effects of reversing monsoons, variations in bathymetry, and river discharge.

During winter, the northeasterly monsoon causes strong cooling and stirring in the shallow coastal sea and induces a southward intrusion of northern cold water along the coast. Consequently, the water temperature is lower in the shallow water near the shore (water depth <30 m) than in the open water (water depth >50 m) (Fig. 1). Therefore, the SST front covering the shallow coastal area formed between the 20 m and 50 m isobaths, parallel to the coastline of southeastern China (Fig. 2).

During summer, the prevailing southwesterly monsoon causes offshore transport of coastal water, favoring the formation of upwelling systems in the NSCS (Xie et al., 2003, Wang et al., 2012) and the northeastward movement of a fresh water plume from the Pearl River estuary (Gan et al., 2009). In relation to these two processes, summer fronts appear in June, mature in July and August, and weaken in September because of the retreat of the summer monsoon.

The differences between the sea surface wind observed by QuikSCAT and simulated by the WRF model may be caused by the overestimation or underestimation of the QuikSCAT equivalent neutral winds in the different stable conditions. For stable conditions, the equivalent neutral wind speeds are smaller than the real wind speeds at 10 m height. For unstable conditions, such as the cold northeasterly winds blowing over the warm water in the NSCS in winter, the equivalent neutral wind speeds are greater than the real wind speeds at 10 m depth (Perlin et al., 2004).

The coupling coefficients calculated by the simulated 10-m real winds of the WRF model are smaller than those calculated by the observed 10-m equivalent neutral winds of QuikSCAT (Table 2). This discrepancy was also discussed in previous studies using numerical models (Song et al., 2009) and buoy observations (O′Neill, 2012). Such a difference was found to occur due to the difference between the 10-m height real winds and equivalent neutral winds under different stable conditions. In addition, the coupling coefficients observed by QuikSCAT reflect a two-way coupling of SST and wind, although QuikSCAT has a low sampling frequency of twice in one day. However, the simulation of the WRF model is a one-way coupling simulation that does not include the response of the oceanic processes to the change of sea surface wind. Thus, the simplification in our simulation for a fully-coupling of SST and wind could also be responsible for differences in the coupling coefficients.

Using the consecutive wind data of QuikSCAT and ASCAT from 2006 to 2011, the same SST–wind couplings at the frontal area of the NSCS are also observed in other years (Fig. 9), but the coupling coefficients differ from year to year (Table 3). The SST–wind coupling coefficient was more notable in 2008 than in other years. This is why we chose 2008 as the representative year to study the influence of a front on surface winds and its seasonal variation in

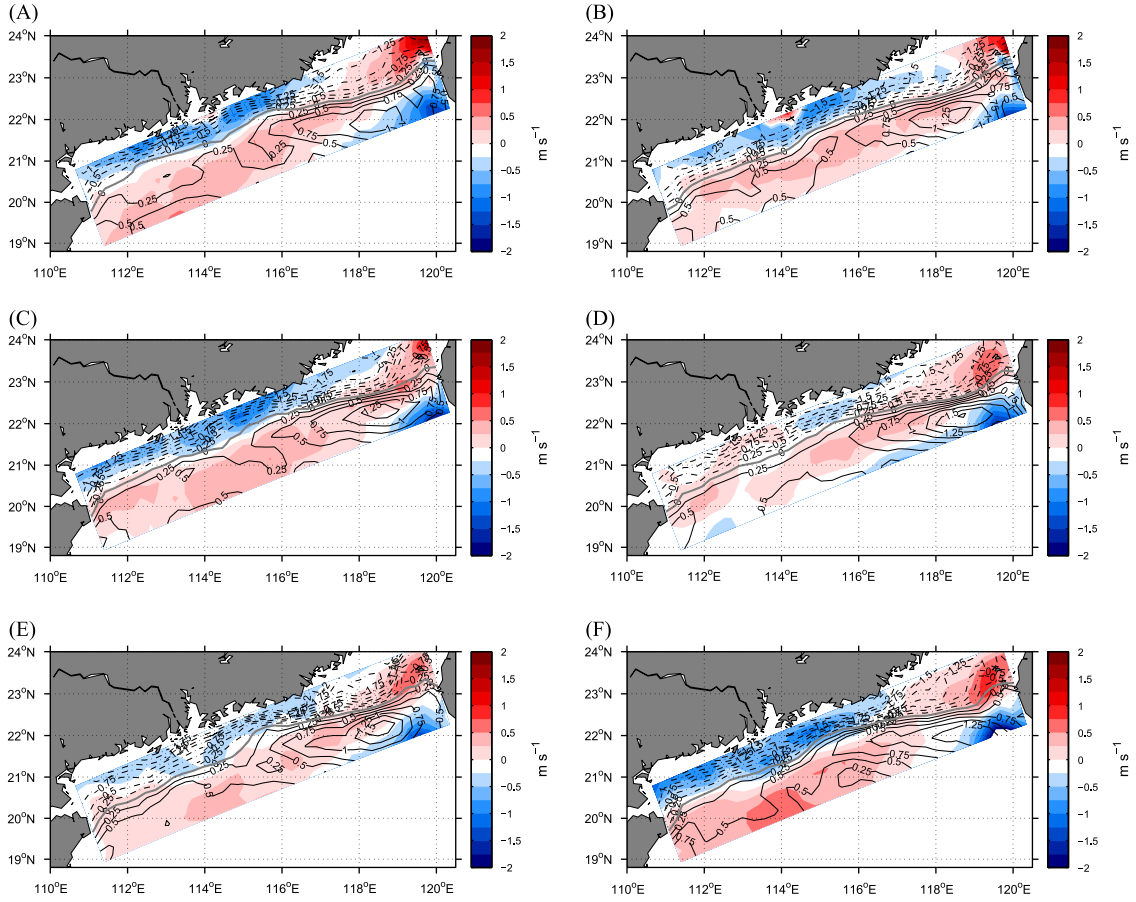

Fig. 9. Same as Fig. 5 but for the monthly mean values of the QuikSCAT (A, B, C) and ASCAT (D, E, F) equivalent neutral wind speeds (m s^{-1}) at 10 m height from December 2006 to December 2011.

Table 3
Coupling coefficients from the scatter plots of the SST and sea surface wind perturbations over the frontal areas in Decembers from 2006 to 2011 (Fig. 8).

Year	2006	2007	2008	2009	2010	2011
Coupling coefficients	0.45	0.34	0.46	0.10	0.20	0.39

this paper. The cause of this yearly variation in the SST–wind coupling is a topic that is currently being discussed and will be investigated in a future study.

5. Summary and conclusion

The OSTIA SST with high resolution was used to investigate the seasonal variations of the oceanic front in the coastal area of the NSCS. The climatological mean of the SST gradient showed that the coastal fronts primarily formed in Beibu Bay, off the northwest coast of Luzon Island, and along the SCC (Figs. 1 and 2).

The SST front can be observed in the SCC throughout the year. Its coverage is much smaller during the summer than in winter, with an abrupt reduction in the covering rate from 80% to 40% in May. The annual minimum covering rate was 20% in September. The monthly mean of the magnitude of the SST gradient associated with the well-developed front was about 0.021 $^{\circ}C\,km^{-1}$ in winter and 0.017 $^{\circ}C\,km^{-1}$ in summer. The annual minimum magnitude of the mean SST gradient in the SCC was approximately 0.011 $^{\circ}C\,km^{-1}$ in October.

The one-year realistic simulation in 2008 by the WRF model (without assimilation) was verified by comparing its results to those of the QuikSCAT observations. The WRF model successfully simulated the spatial pattern of the monthly sea surface wind magnitude and direction in the NSCS in 2008. The small RMSDs of the 10 m height wind speeds and MEANs of the 10 m height wind direction demonstrated the efficiency of the model in simulating the response of surface wind to the SST perturbations associated with the oceanic front.

Both the satellite observations and WRF model exhibited a positive linear correlation between the spatially high-pass-filtered surface wind and SST, indicating the local influence of the coastal SST front on the sea surface wind in the NSCS. The SST–wind coupling coefficients calculated from the SST–wind linear correlation are larger in the NSCS than those observed over the Gulf Stream, but smaller than those observed over the equatorial Pacific.

The local influence of the coastal SST front on the sea surface wind was overlaid by the narrowing effect and blocking of the topography at the southern end of the Taiwan Strait due to the northeast monsoon during the winter. In summer, the influence of the SST front on the sea surface wind becomes significant along the southern end of the Taiwan Strait due to the reversing of the monsoon. The transition of a monsoon could also affect the SST–wind coupling in the NSCS.

The SST–wind coupling discussed in this paper only reflects the influence of the ocean on the atmosphere. The feedback of the ocean to the change in the atmosphere is taken into account. The response of the sea surface wind to the SST front may significantly influence the underlying fronts. We will examine this issue in a subsequent study by using an air-sea coupled model.

Acknowledgments

This study was supported by the National Natural Basic research Program of China (973 Program, no. 2011CB403501), the National Natural Science Foundation of China (nos. 41106028 and 41206011), the Knowledge Innovation Project for Distinguished Young Scholars of the Chinese Academy of Sciences (no. KZCX2-EWQN203), and the Knowledge Innovation Program of the Chinese Academy of Sciences (no. 54-SQ201104-1), Project on the Integration of Industry, Education and Research of Guangdong Province (no. 20110908). This study was also partly supported by Grants-in-Aid for Scientific Research (22106002) from the Ministry of Education, Culture, Sports, Science and Technology, Japan. The numerical simulation is supported by the high-performance computing division and Ms. Dandan Sui of the South China Sea Institute of Oceanology.

References

Belkin, I.M., Comillon, P.C., Sherman, K., 2009. Fronts in large marine ecosystems. Prog. Oceanogr. 81, 223–236.
Cayan, D.R., 1992. Latent and sensible heat flux anomalies over the northern oceans: driving the sea surface temperature. J. Phys. Oceanogr. 22, 859–881.
Chelton, D.B., Esbensen, S.K., Schlax, M.G., Thum, N., Freilich, M.H., Wentz, F.J., Gentemann, C.L., McPhaden, M.J., Schopf, P.S., 2001. Observations of coupling between surface wind stress and sea surface temperature in the Eastern Tropical Pacific. J. Clim. 14, 1479–1498.
Chelton, D.B., Schlax, M.G., Freilich, M.H., Milliff, R.F., 2004. Satellite measurements reveal persistent small-scale features in ocean winds. Science 303, 978–983.
Chelton, D.B., Wentz, F.J., 2005. Global microwave satellite observations of sea-surface temperature for numerical weather prediction and climate research. Bull. Am. Meteor. Soc. 86, 1097–1115.
Chelton, D.B., Xie, S.-P., 2010. Coupled ocean–atmosphere interaction at oceanic mesoscales. Oceanography 23, 52–69.
Gan, J., Li, L., Wang, D., Guo, X., 2009. Interaction of a river plume with coastal upwelling in the northeastern South China Sea. Cont. Shelf Res. 29, 728–740.
Hayes, S.P., MaPhaden, M.J., Wallace, J.M., 1989. The influence of sea surface temperature on surface wind in the eastern equatorial Pacific: weekly to monthly variability. J Clim. 2, 1500–1506.
Hu, J.Y., Kawamura, H., Tang, D.L., 2003. Tidal front around the Hainan Island, northwest of the South China Sea. J. Geophys. Res. 108 (C11), 3342, http://dx.doi.org/10.1029/2003JC001883.
Lindzen, R., Nigam, S., 1987. On the role of sea surface temperature gradients in forcing low-level winds and convergence in the Tropics. J. Atmos. Sci. 44, 2418–2436.
Liu, S., Guo, X., Chen, Q., Bi, Y., Zhang, J., Ng, W., Luo, X., Li, J., 2010. Nutrient dynamics in the thermohaline frontal zone of the northern shelf region of the South China Sea. J. Geophys. Res. 115, C11020, http://dx.doi.org/10.1029/2009JC005951.
Mellor, G.L., Yamada, T., 1982. Development of a turbulence closure model for geophysical fluid problems. Rev. Geophys. Space Phys. 20, 851–875.
Nakanishi, M., Niino, H., 2006. An improved Mellor–Yamada level-3 model: its numerical stability and application to a regional prediction of advection fog. Boundary-Layer Meteorol. 119, 397–407.
Nonaka, M., Xie, S.P., 2003. Covariations of sea surface temperature and wind over the Kuroshio and its extension: evidence for ocean-to-atmosphere feedback. J. Clim. 16, 1404–1413.
O'Neill, L.W., Chelton, D.B., Esbensen, S.K., Wentz, F.J., 2005. High-resolution satellite measurements of the atmospheric boundary layer response to SST variations along the Agulhas return current. J. Clim. 18, 2706–2723.
O'Neill, L.W., Esbensen, S.K., Thum, N., Samelson, R.M., Chelton, D.B., 2010. Dynamical analysis of the boundary layer and surface wind responses to mesoscale SST perturbations. J. Clim. 23, 559–581.
O'Neill, L.W., 2012. Wind speed and stability effects on coupling between surface wind stress and SST observed from buoys and satellite. J. Clim. 25, 1544–1569.
Perlin, N., Samelson, R.M., Chelton, D.B., 2004. Scatterometer and model wind and wind stress in the Oregon–Northern California coastal zone. Mon. Weather Rev. 132, 2110–2129.
Samelson, R.M., Skyllingstad, E.D., Chelton, D.B., Esbensen, S.K., O'Neill, L.W., Thum, N., 2006. On the coupling of wind stress and sea surface temperature. J. Clim. 19, 1557–1566.
Skamarock, W.C., Klemp, J.B., Dudhia, J., Gill, D.O., Barker, D.M., Wang, W., Powers, J. G., 2005. A Description of the Advanced Research WRF Version 2. NCAR Tech. Note NCAR/TN4681STR, NCAR, pp. 88.
Small, R.J., Xie, S.-P., Wang, Y., 2003. Numerical simulation of atmospheric response to Pacific tropical instability waves. J. Clim. 16, 3722–3740.
Small, R.J., deSzoeke, S.P., Xie, S.-P., O'Neill, L., Seo, H., Song, Q., Cornillon, P., Spall, M., Minobe, S., 2008. Air–sea interaction over ocean fronts and eddies. Dyn. Atmos. Oceans 45, 274–319.
Song, Q., Cornillon, P., Hara, T., 2006. Surface wind response to oceanic fronts. J. Geophys. Res. 111 (C12), C12006.
Song, Q., Chelton, D.B., Esbensen, S.K., Thum, N., O'Neill, L.W., 2009. Coupling between sea surface temperature and low-level winds in mesoscale numerical models. J. Clim. 22, 146–164.
Stark, J.D., Donlon, C.J., Martin, M.J., McCulloch, M.E., 2007. OSTIA: an operational, high resolution, real time, global sea surface temperature analysis system. In:

IEEE/OES Proceedings of Oceans 2007, Marine Challenges: Coastline to Deep Sea, Aberdeen, Scotland, pp. 1–4.
Tanimoto, Y., Kanenari, T., Tokinaga, H., Xie, S.-P., 2011. Sea level pressure minimum along the Kuroshio and its extension. J. Clim. 24, 4419–4434.
Tokinaga, H., Tanimoto, Y., Xie, S.-P., 2005. SST-induced surface wind variations over the Brazil–Malvinas confluence: satellite and in situ observations. J. Clim. 18, 3470–3482.
Tokinaga, H., Tanimoto, Y., Nonaka, M., Taguchi, B., Fukamachi, T., Xie, S.-P., Nakamura, H., Watanabe, T., Yasuda, I., 2006. Atmospheric sounding over the winter Kuroshio Extension: effect of surface stability on atmospheric boundary layer structure. Geophys. Res. Lett. 33, L04703, http://dx.doi.org/10.1029/2005GL025102.
Wallace, J.M., Mitchell, T.P., Deser, C., 1989. The influence of sea surface temperature on surface wind in the eastern equatorial Pacific: seasonal and interannual variability. J. Clim. 2, 1492–1499.
Wang, D., Liu, Y., Qi, Y., Shi, P., 2001. Seasonal variability of thermal fronts in the northern South China Sea from satellite data. Geophys. Res. Lett. 28, 3963–3966, http://dx.doi.org/10.1029/2001GL013306.
Wang, D., Zhuang, W., Xie, S.-P., Hu, J., Shu, Y., Wu, R., 2012. Coastal upwelling in summer 2000 in the northeastern South China Sea. J. Geophys. Res. 117, C04009, http://dx.doi.org/10.1029/2011JC007465.
Xie, J., Zhu, J., Li, Y., 2008. Assessment and inter-comparison of five high-resolution sea surface temperature products in the shelf and coastal seas around China. Cont. Shelf Res. 28, 1286–1293.
Xie, S.-P., Xie, Q., Wang, D., Liu, W.T., 2003. Summer upwelling in the South China Sea and its role in regional climate variations. J. Geophys. Res. 108 (C8), 3261, http://dx.doi.org/10.1029/2003JC001867.
Xie, S.-P., 2004. Satellite observations of cool ocean–atmosphere interaction. Bull. Am. Meteor. Soc. 85, 195–208.
Yanagi, T., Koike, T., 1987. Seasonal variation in thermohaline and tidal fronts, Seto Inland Sea, Japan. Cont. Shelf Res. 7, 149–160.